

# Journal of Biomedical Optics

[SPIEDigitalLibrary.org/jbo](http://SPIEDigitalLibrary.org/jbo)

## **High-sensitivity, real-time, ratiometric imaging of surface-enhanced Raman scattering nanoparticles with a clinically translatable Raman endoscope device**

Ellis Garai  
Steven Sensarn  
Cristina L. Zavaleta  
Dominique Van de Sompel  
Nathan O. Loewke  
Michael J. Mandella  
Sanjiv S. Gambhir  
Christopher H. Contag

# High-sensitivity, real-time, ratiometric imaging of surface-enhanced Raman scattering nanoparticles with a clinically translatable Raman endoscope device

Ellis Garai,<sup>a,g</sup> Steven Sensarn,<sup>b,c,g</sup> Cristina L. Zavaleta,<sup>b,g</sup> Dominique Van de Sompel,<sup>b,g</sup> Nathan O. Loewke,<sup>f,g</sup> Michael J. Mandella,<sup>c,g</sup> Sanjiv S. Gambhir,<sup>b,d,g</sup> and Christopher H. Contag<sup>b,c,e,g</sup>

<sup>a</sup>Stanford University, Department of Mechanical Engineering, Stanford, California 94305

<sup>b</sup>Stanford University, Department of Radiology, Stanford, California 94305

<sup>c</sup>Stanford University, Department of Pediatrics, Stanford, California 94305

<sup>d</sup>Stanford University, Departments of Bioengineering and Materials Science and Engineering, Stanford, California 94305

<sup>e</sup>Stanford University, Department of Microbiology & Immunology, Stanford, California 94305

<sup>f</sup>Stanford University, Department of Electrical Engineering, Stanford, California 94305

<sup>g</sup>Stanford University, Molecular Imaging Program at Stanford, Stanford, California 94305

**Abstract.** Topical application and quantification of targeted, surface-enhanced Raman scattering (SERS) nanoparticles offer a new technique that has the potential for early detection of epithelial cancers of hollow organs. Although less toxic than intravenous delivery, the additional washing required to remove unbound nanoparticles cannot necessarily eliminate nonspecific pooling. Therefore, we developed a real-time, ratiometric imaging technique to determine the relative concentrations of at least two spectrally unique nanoparticle types, where one serves as a nontargeted control. This approach improves the specific detection of bound, targeted nanoparticles by adjusting for working distance and for any nonspecific accumulation following washing. We engineered hardware and software to acquire SERS signals and ratios in real time and display them via a graphical user interface. We report quantitative, ratiometric imaging with nanoparticles at pM and sub-pM concentrations and at varying working distances, up to 50 mm. Additionally, we discuss optimization of a Raman endoscope by evaluating the effects of lens material and fiber coating on background noise, and theoretically modeling and simulating collection efficiency at various working distances. This work will enable the development of a clinically translatable, noncontact Raman endoscope capable of rapidly scanning large, topographically complex tissue surfaces for small and otherwise hard to detect lesions. © The Authors. Published by SPIE under a Creative Commons Attribution 3.0 Unported License. Distribution or reproduction of this work in whole or in part requires full attribution of the original publication, including its DOI. [DOI: [10.1117/1.JBO.18.9.096008](https://doi.org/10.1117/1.JBO.18.9.096008)]

Keywords: Raman spectroscopy; Raman effect; endoscopy; real-time imaging; optical devices; optical design.

Paper 130349R received May 14, 2013; revised manuscript received Jul. 24, 2013; accepted for publication Jul. 31, 2013; published online Sep. 5, 2013.

## 1 Introduction

The mucosal surface of hollow organs is a region that can be infiltrated by various cancers. Although the current standard of patient monitoring—white-light endoscopy—has greatly advanced the ability to detect disease, novel endoscope-compatible instruments and molecular imaging agents are needed for point-of-care diagnosis and treatment. In the United States, over 50,000 lives are lost annually to colon cancer alone, making it the third deadliest cancer.<sup>1</sup> Worldwide, colorectal cancer has the third highest mortality rate and the fourth highest incidence rate.<sup>2</sup> These statistics demonstrate the necessity for novel tools to diagnose early epithelial cancers in hollow organs. This is particularly true for detection of flat lesions in the colon, which are more commonly missed with conventional white light endoscopy.<sup>3</sup> Topical application of functionalized surface-enhanced Raman scattering (SERS) nanoparticles and detection with an endoscope-deployable, fiber-based SERS endoscope comprise a molecular imaging technology with potential for early detection of epithelial cancers in hollow

organs.<sup>4,5</sup> In addition to enabling detection of early and flat lesions invisible to camera-based endoscopy, advances in these technologies will allow endoscopists to better identify margins for tumor resection to prevent tumor recurrence.

SERS nanoparticles provide the potential to enable Raman spectroscopy as a molecular imaging modality. These nanoparticles consist of Raman-active molecules adsorbed onto a metal core, which provides for significant Raman enhancement due to the generation of plasmon resonance on the surface of the metallic core.<sup>6–9</sup> The enhancement factor can be as large as  $10^{14}$  to  $10^{15}$ , which allows for a higher SNR and ultimately enhances the sensitivity of detection.<sup>6,10–12</sup> When illuminated by a 785-nm laser, the SERS nanoparticles generate narrow-band spectral peaks in the near-infrared. Depending on the particular Raman-active layer adsorbed onto the gold core, each type of SERS nanoparticle, or flavor, generates a unique spectral signature that enables multiplexing.<sup>13,14</sup> While not all SERS nanoparticles have reproducible spectra, the SERS nanoparticles that we use (provided by Cabot Corp., formerly Oxonica Materials Inc., Mountain View, California) are unique in that they are highly reproducible. Additionally, unlike fluorescent probes, SERS nanoparticles do not photobleach, which results in a reproducible, stable signal over time.<sup>13,15</sup> Significantly, the large size of the SERS nanoparticles (120 nm) prevents them from entering the systemic circulation following topical application to the

Address all correspondence to: Sanjiv S. Gambhir, Stanford University, 318 Campus Drive, Clark Center, Rm E150, Stanford, California, 94305. E-mail: [sgambhir@stanford.edu](mailto:sgambhir@stanford.edu); Christopher H. Contag, Stanford University, 318 Campus Drive, Clark Center, Rm E150, Stanford, California, 94305. Tel: 650-725-6583; Fax: (650) 498-7723; E-mail: [ccontag@stanford.edu](mailto:ccontag@stanford.edu)

colon wall, and possibly the inner walls of other hollow organs. Several studies have been recently published describing the biodistribution and toxicity effects of SERS nanoparticles and the likely reduction of toxicity through the use of intrarectal—as opposed to intravenous—administration in animal models.<sup>16–18</sup>

Fiber-bundle-based devices that measure the intrinsic Raman signal—as opposed to exogenous SERS signals—of a given tissue have been developed and have demonstrated sufficient sensitivity for various clinical applications.<sup>19–29</sup> Some of these designs incorporate an illumination fiber surrounded by collection fibers.<sup>19,23,24,27</sup> The Nie and Wilson groups have each developed fiber-based systems to detect SERS nanoparticles as exogenous contrast agents for clinical use. Nie et al. describe a hand-held spectroscopic pen device that can detect SERS nanoparticles.<sup>30</sup> Wilson and colleagues describe an SERS endoscope system that modifies a current clinical endoscope<sup>31–33</sup> and uses a scanning bandpass filter to quantify the Raman signal at individual wavelengths, allowing sequential imaging of four SERS nanoparticle flavors.

Building on these advances, we recently reported on a non-contact Raman endoscope device that is able to scan large areas quickly, and we have demonstrated that this device can identify and quantify SERS particles in a mixture of up to 10 flavors.<sup>34</sup> There are, however, several important characteristics that must also be met in order for such a detection system to be fully clinically translatable, in addition to having the ability to quickly scan large surface areas.

First, the device must be able to detect low, clinically relevant concentrations of various mixtures of SERS nanoparticles. Improved sensitivity to the detection of SERS nanoparticles can be achieved through a reduction of background signal generated in the detection system and through improved algorithms used to extract the SERS signal from noise. Reduction in noise of the system can be achieved by optimizing the optical design and through the selection of appropriate optical components and materials. In regards to SERS signal extraction, several strategies have been previously employed to identify the SERS signal from a given acquisition, but each has its respective set of limitations. Filtering approaches, such as bandpass filtering algorithms, have been previously developed and used for this purpose.<sup>31</sup> A least-squares algorithm has been previously described to extract signals by fitting a set of known Raman and background references to a measurement.<sup>35</sup> It would be advantageous to obtain a large data set of the colon wall, for example, prior to the topical application of the SERS nanoparticles in order to optimally characterize the background signal. However, in the clinical setting, it may be impractical to provide the entire background set to a filter-based or least-squares algorithm in real time, as it would be computationally expensive. We address this limitation through the use of a custom algorithm that utilizes a combination of least-squares and principal component analysis (PCA) to extract the distinguishing characteristics of the background.

Second, the distance of the device from the surface being interrogated should not cause a variation in the detected signal. However, the absolute value of the Raman scattering signal decreases as working distance increases. In clinical practice, it is beneficial for the signal to remain relatively constant as the working distance changes, since it is difficult for a physician to hold the endoscope perfectly still.

Last, topical application of the SERS nanoparticles, while less toxic than intravenous administration, requires a washing

step to remove unbound nanoparticles. This step is imperfect in that it reduces, but does not eliminate, random pooling of unbound targeted and untargeted nanoparticles. In previous utilizations of SERS nanoparticles, no additional flavors were used as a control to account for nonspecific signal.<sup>13,14,31,36</sup>

To address the last two limitations, our clinically oriented strategy uses a ratiometric approach for quantifying at least two SERS nanoparticle flavors, where one is used as a nontargeted reference for internal control, and one or more flavors is used to target a relevant cell surface protein. Multiple targeted particles may be useful to simultaneously image multiple genetic markers to improve specificity for various clinical applications.

We and others have previously used a ratiometric approach with fluorophores to improve detection of molecular targets.<sup>37–39</sup> We reasoned that a similar method could be used with our SERS nanoparticles. One flavor of the SERS nanoparticles could be coated with tumor-specific ligand(s) such as antibodies, affibodies, or peptides that bind to a specific tumor tissue expressing the corresponding cell surface protein. Then, another nanoparticle flavor could act as the control to account for nonspecific binding and pooling within the colon. This nanoparticle flavor would remain nonspecific by, for instance, coating it with a random control sequence peptide having a moiety of similar molecular composition. The ratio of targeted-to-control Raman signal represents the relative quantity of cell surface proteins present and is independent of working distance. We also reasoned that ratiometric imaging could be more robust with SERS nanoparticles than with fluorophores due to the sharp, spectrally separated emission patterns of the nanoparticles compared to the broad, overlapping spectral distributions that would typically occur when detecting a mixture of different fluorophores.

Following topical application, the tissue would be washed to remove a majority of the unbound nanoparticles, the device would be inserted into the working channel of a commercial endoscope, and the remaining SERS nanoparticles would then be detected and quantified. The data are then processed and reported in real time with the intent of determining what pathological conditions exist based on the identified location and quantification of bound targeted SERS nanoparticles relative to the retention of nontargeted, control nanoparticles. The system described below can unambiguously detect and quantify the presence of up to 10 flavors of SERS nanoparticles simultaneously, without having to separately image each flavor. The multiplexing capabilities of SERS nanoparticles, our device, and our customized software enable the data to be processed and reported instantly to identify pathological conditions. Thus, the system can be used for point-of-care diagnosis and guiding immediate treatment strategies.

To our knowledge, this is the first published discussion of ratiometric imaging with SERS nanoparticles. Prior to this technique, the nonspecific accumulation of topically applied SERS nanoparticles following washing limited its usefulness in detecting targeted, bound nanoparticles. With our technique, nonspecific nanoparticle accumulation is accounted for using our nontargeted control flavor; locations where the targeted flavor is over-represented, relative to the nontargeted flavor, indicate the presence of cells expressing the corresponding cell surface protein of interest (i.e., tumor tissue).

Here we further detail the optimization and characterization of the device for the detection of nanoparticles in the mid-femto to low picomolar range, generate and compare computational simulations to experimental results, introduce a ratiometric

approach for maintaining a stable signal level over large working distances, and demonstrate real-time ratiometric imaging using a custom graphical user interface (GUI). Since functionalized SERS nanoparticles have previously been demonstrated,<sup>4,36,40,41</sup> the current study was designed to optimize their detection and demonstrate clinical relevance.

## 2 Material and Methods

### 2.1 High-Level System Design

The design of the Raman endoscope was based on a previous forward-looking implementation.<sup>34</sup> The fiber bundle system

consists of a continuous-wave laser centered at 785 nm coupled into a single-mode fiber housed within a fiber bundle. The distal end of the fiber bundle consists of a centrally located single-mode illumination fiber surrounded by 36 multimode collection fibers, which are arranged in a hexagonal pattern allowing for collinear illumination and Raman collection. A plano-convex lens is used to collimate the illumination beam from the single-mode fiber and collect the Raman scattered light into the multimode fibers [Fig. 1(a)]. The proximal end consists of 36 multimode collection fibers arranged in a linear array, which is then coupled into a spectrometer. Others have arranged the collection fiber array into a parabolic arc to improve the SNR and spectral resolution of the system.<sup>23</sup> This is an important

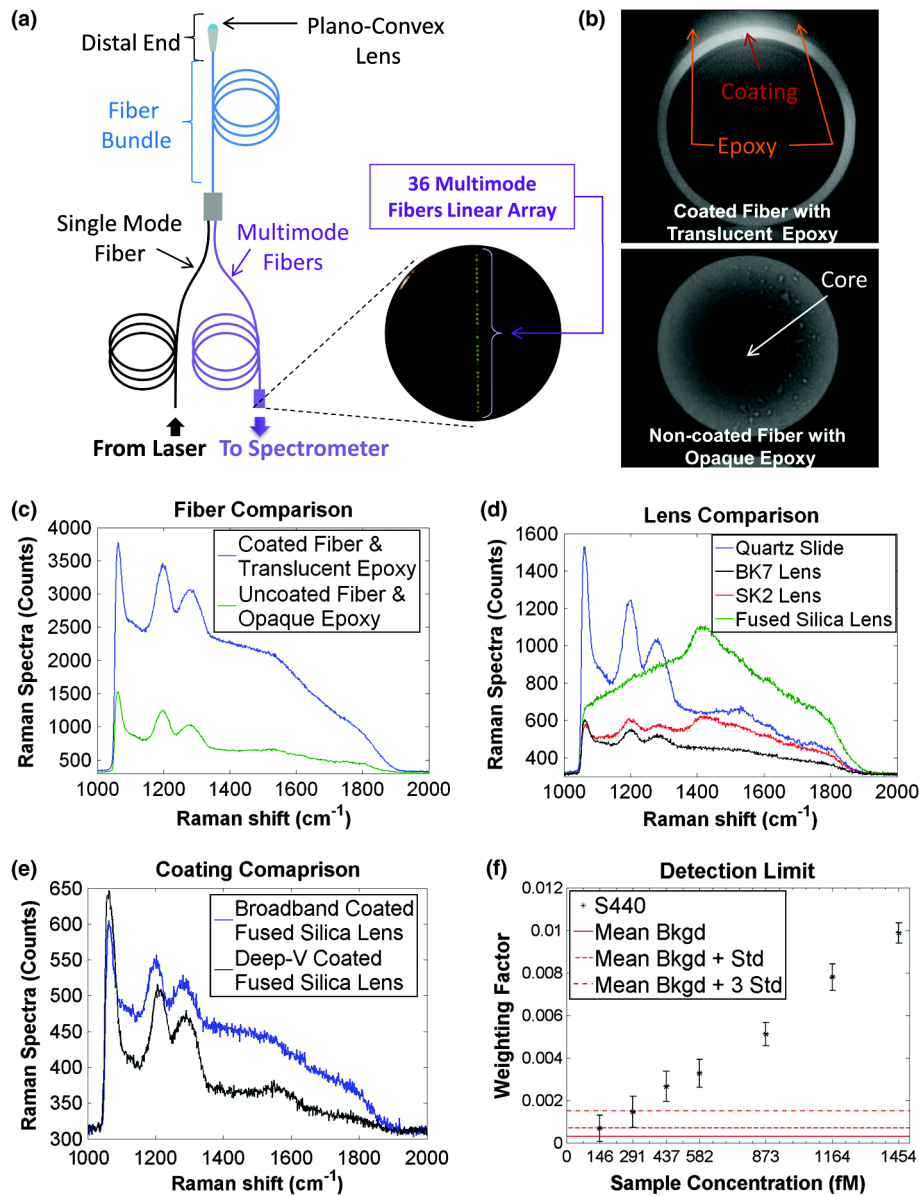


**Fig. 1** (a) Schematic of the fiber bundle assembly. (b) An image of one of the multimode fibers from the 36-fiber linear array after illumination by a laser and filtering by a long-pass filter (image of intrinsic fluorescence/Raman noise). Top: epoxy between multimode fibers as well as the polyimide fiber coating result in background noise captured by the spectrometer. Bottom: an alternative fiber bundle configuration with the coatings of the multimode fibers removed at the proximal end. The multimode fibers were assembled with opaque epoxy. Intrinsic noise is generated only in the pure-silica fiber core. (c) A comparison of background noise spectra using the two different fiber bundle configurations, described in (b), when sampling a quartz slide. (d) Comparison of background noise spectra using various lens materials (BK7, SK2, and fused silica) with the improved, uncoated fiber bundle. (e) A deep-V, anti-reflection coating helps mitigate background noise. (f) Detection limit measurements with optimized fiber bundle and lens.

consideration for collecting intrinsic Raman signals when software binning is used or when it is necessary to resolve Raman spectra of interest. However, because we are detecting SERS nanoparticles with hardware (full vertical) binning, our SNR would not improve by compensating for the arc, and we find that the slight arc on a CCD camera in our system does not significantly broaden the spectral signatures of the nanoparticles.

The spectrometer contains an 830-nm long-pass filter to block any illumination light from the laser at 785 nm, which would otherwise result in background noise. The spectrometer disperses the wavelengths of light (830 to 930 nm) onto a two-dimensional, deep-depleted CCD array (Andor, Belfast, UK). The electronics internal to the CCD perform full vertical binning (FVB) of the sensory elements to sum the spectral intensities at each wavelength, resulting in the production of Raman spectra. Each Raman spectrum, which is referred to as an acquisition when integrated over a given period of time, is then entered into an algorithm to extract the Raman signal associated with each SERS flavor.

### 2.2 Optimization of the Raman Endoscope

In order to optimize the device and reduce the background noise generated within our system, various measurements were performed to test any noise that may be generated by the optical components.

First, laser light was directed into 36 multimode fibers, and one of the fibers was imaged at the proximal end via a microscope objective and monochrome CCD [Fig. 1(b) top]. A long-pass filter was placed in front of the CCD to block the laser light. Red-shifted light was observed exiting the coating of the multimode fiber as well as the epoxy surrounding the fibers; the polyimide coating and transparent epoxy were independently generating Raman/fluorescence signal and contributing to background noise. To eliminate this noise, a new fiber bundle was designed where the coating around the multimode fibers at the proximal end of the fiber bundle was removed, and the transparent epoxy was replaced with an opaque alternative [Fig. 1(b) bottom]. The original fiber bundle with the coated multimode fibers and transparent epoxy was compared to the newly designed fiber bundle with the uncoated multimode fibers and opaque epoxy [Fig. 1(c)]. To compare the bundles, a quartz microscope slide was placed 5 mm from the distal end of the fiber bundle and perpendicular to the optic axis; the background signal of each fiber bundle configuration was then measured. An integration time of 500 ms and an output power from the device of 40 mW were used.

Second, various lens materials and lens coating were tested for levels of Raman scattering that would contribute to the background signal of the system [Figs. 1(d) and 1(e)]. Tested materials included quartz, BK7, SK2, and fused silica. Each lens type was placed one focal length away from the distal end of the fiber bundle. An integration time of 500 ms and an output power of 40 mW were used.

### 2.3 Limit of Detection

To determine the limit of detection, 3 mL of various concentrations of SERS nanoparticles ranging from 146 to 1454 fM were imaged in 9.5-cm<sup>2</sup> wells [Fig. 1(f)]. 2-(*N*-morpholino) ethanesulfonic acid (MES) was used to dilute the SERS nanoparticles to the desired concentrations; thus, the background level was established using MES. For each sample, a series

of 25 acquisitions were taken in a rectangular pattern in different locations of the well creating a 5 × 5 array having 1.00 mm steps. The CCD was set to a gain of 4× with an integration time of 300 ms, and the output of the device was set to 60 mW. These settings resulted in an illumination power that is below American National Standards Institute limit for maximum permissible exposure.

### 2.4 Collection Efficiency Simulations

FRED software (Version 11.90.2, Photon Engineering, Tucson, AZ) was used to model the newly designed optical system at the distal end of the device and to simulate Raman-scattered light [Figs. 2(b) and 2(c)]. A custom-machined, stainless-steel lens holder retains the fused-silica, deep-V antireflection-coated plano-convex lens (CVI Melles Griot, P/N: PLCX-4.0-3.1-UV) at a distance of one focal length away from the fiber bundle plane. The lens has a 4.00-mm diameter, a 1.5-mm center

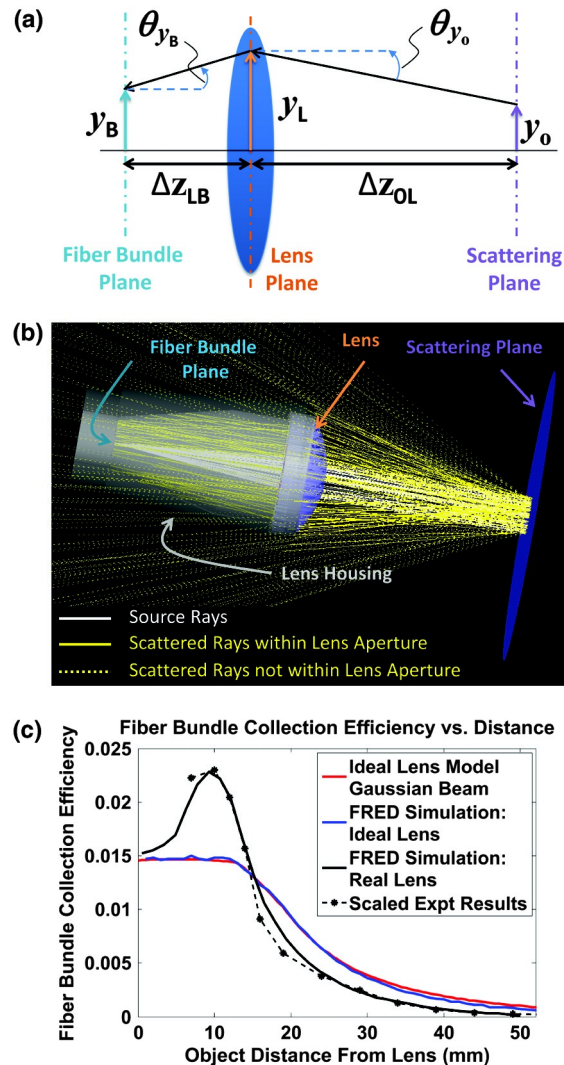


**Fig. 2** (a) Schematic of ideal lens model and variables used for analysis. (b) FRED simulation of the distal end of the fiber bundle assembly. (c) Comparison of the FRED simulation (both real and ideal lens) and Eq. (2) (ideal lens). The points shown are the experimentally measured Raman signal scaled to fit the FRED model. To avoid contact with the SERS solution, the distal end of the device was brought no closer than ~7 mm.

thickness, and a focal length of 6.83 mm at 785 nm. The white rays illustrated in Fig. 2(b) represent rays emitted from the single-mode illumination fiber at the center of the fiber bundle and are collimated by the plano-convex lens. The rays are then scattered off of the scattering plane. The scattered light is modeled with a Lambertian profile<sup>42</sup> to mimic the ideal scattering of a layer of SERS nanoparticles. The solid yellow lines illustrated in Fig. 2(b) represent rays that are scattered from the scattering plane and that fall within the aperture of the lens. A subset of these rays falls within the aperture of the fiber bundle, and a subset of those rays falls within the acceptance angle of each of the 36 multimode fibers. The fiber bundle plane was modeled by an annular region having an outside diameter of 1.7 mm and an inside diameter of 300  $\mu\text{m}$  to represent the area occupied by the multimode fibers. The fiber bundle plane's inside diameter is 300  $\mu\text{m}$  due to the single-mode illumination fiber occupying the central region. Using a Gaussian model, the FRED simulation predicts an average  $1/e^2$ -intensity diameter of the collimated beam to be 1.42 mm in a range of working distances, between 0 and 60 mm, from the surface of the lens. Experimentally, the collimated beam of the device was measured using a beam scanner (Photon, BeamScan<sup>TM</sup>) over this range of working distances. The profile of the beam over this range matched closely to an ideal Gaussian profile with an average  $1/e^2$  diameter of 1.408 mm along the  $x$  axis and an average  $1/e^2$  diameter of 1.422 mm along the  $y$  axis. Thus, the average  $1/e^2$  diameter

was 1.415 mm across both axes over this range of working distances.

In order to confirm the results from the FRED simulations, a simplified model was developed as a comparison, using an ideal lens as described by the diagram shown in Fig. 2(a). For this numerical model, rays are propagated from the scattering object (subscript  $o$ ) to the lens (subscript  $L$ ) and from the lens to the fiber bundle (subscript  $B$ ).

$$\begin{aligned} x_L &= x_o + \Delta z_{oL} \tan(\theta_o) \cos(\phi_o), \\ \theta_{x_B} &= \tan^{-1} \left[ \tan(\theta_o) \cos(\phi_o) - \frac{x_L}{f} \right], \\ x_B &= x_L + \Delta z_{LB} \tan(\theta_{x_B}), \\ y_L &= y_o + \Delta z_{oL} \tan(\theta_o) \sin(\phi_o), \\ \theta_{y_B} &= \tan^{-1} \left[ \tan(\theta_o) \sin(\phi_o) - \frac{y_L}{f} \right], \\ y_B &= y_L + \Delta z_{LB} \tan(\theta_{y_B}). \end{aligned} \quad (1)$$

From the Lambertian Raman scattering plane, each differential element of projected area,  $dA_o = \cos(\theta_o) dx_o dy_o$ , scatters rays uniformly over all  $\theta_o$  and  $\phi_o$  (elevation and azimuthal angles, respectively). Thus, each ray fills a solid angle of  $d\Omega_o = \sin(\theta_o) d\theta_o d\phi_o$ . The resulting total scattered power,  $P$ , is given by

$$P = \int_0^{2\pi} \int_0^{\pi/2} \int_{-\infty}^{\infty} \int_{-\infty}^{\infty} L(x_o, y_o, \theta_o, \phi_o) C(x_o, y_o, \theta_o, \phi_o) \cos(\theta_o) \sin(\theta_o) dx_o dy_o d\theta_o d\phi_o. \quad (2)$$

The intensity distribution of scattered rays,  $L$ , is defined to match the Gaussian profile of the laser beam, having  $1/e^2$  intensity diameter  $D_s$ , and is normalized to unit power.

$$L(x_o, y_o, \theta_o, \phi_o) = \frac{8}{(\pi D_s)^2} \exp \left[ -2 \left( \frac{\sqrt{x_o^2 + y_o^2}}{D_s/2} \right)^2 \right]. \quad (3)$$

The criteria function  $C$  controls whether a given ray contributes to Raman signal captured by the device and is given by

$$C(x_o, y_o, \theta_o, \phi_o) = \begin{cases} 1 & \text{when rays are captured and guided} \\ 0 & \text{when rays are not captured and not guided} \end{cases} \quad (4)$$

Rays will be captured at the fiber bundle plane and guided to the detector if the following conditions are met:

$$\begin{aligned} \sqrt{x_L^2 + y_L^2} &\leq \frac{D_L}{2}, & \frac{D_{\text{SMF}}}{2} &\leq \sqrt{x_B^2 + y_B^2} \leq \frac{D_B}{2}, \\ \theta_{x_B} &\leq \sin^{-1}(\text{NA}), & \theta_{y_B} &\leq \sin^{-1}(\text{NA}). \end{aligned} \quad (5)$$

$D_B$  is the outside diameter of the area occupied by the multimode fiber bundle,  $D_{\text{SMF}}$  is the diameter of the single-mode fiber at the center of the bundle (within which no scattered light can be collected),  $D_L$  is the lens diameter (4 mm), and NA is the numerical aperture of the multimode fibers. Equation (2) was evaluated numerically at various working distances,  $\Delta z_{oL}$ , using MATLAB software and the results are shown in Fig. 2(c).

## 2.5 Working Distance Collection Efficiency Characterization

The collection efficiency over varied working distances was evaluated and characterized using the following two SERS nanoparticle flavors: S440 and S493 (spectra shown in Fig. 3). The experimental data were scaled to fit the FRED simulation results such that the mean square error was minimized [Fig. 2(c)]. In Fig. 4(a), a 9.5-cm<sup>2</sup> well containing 14-pM S440 and 14-pM S493, in a total volume of about 3 mL, was sampled with the device. In Fig. 4(c), the concentration of S440 was increased to 28 pM (2:1 ratio). Figures 4(b) and 4(d) show

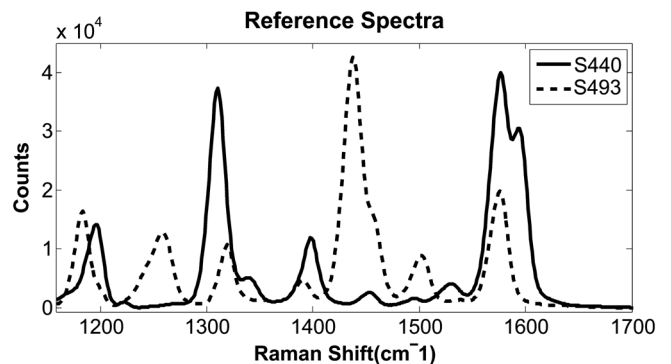


**Fig. 3** Reference spectra of stock concentration (800 pM) of S440 (solid curve) and S493 (dashed curve). Raman-active molecules adsorbed onto the gold core of the SERS nanoparticles lead to the unique spectra of each flavor.

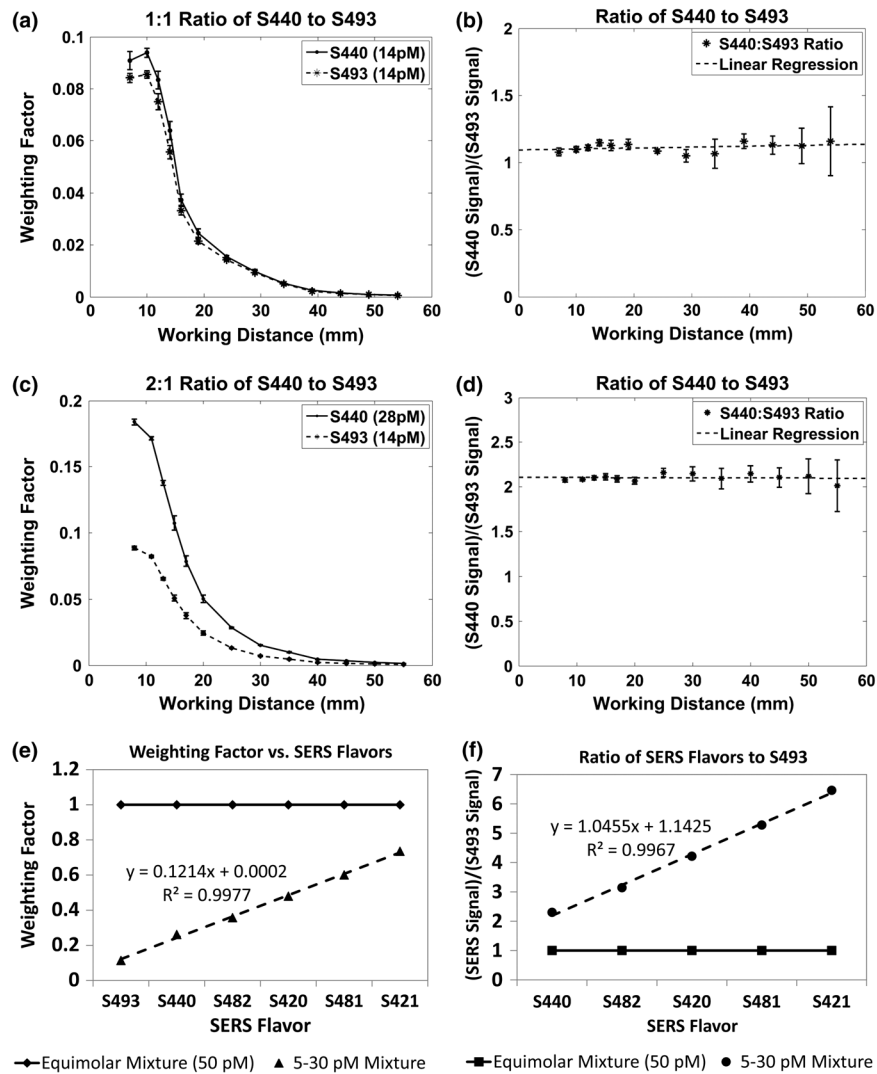


**Fig. 4** (a) Raman signal for S440 (solid curve) and S493 (dashed curve) at varying distances. A 3 mL mixture with 14-pM S440 and 14-pM S493 was imaged in a 9.5-cm<sup>2</sup> well. (b) Measured 1:1 ratio of S440 to S493 signal intensities at varying working distances. (c) Same as (a) but with 28-pM S440 and 14-pM S493. (d) 2:1 measured ratio of S440 to S493 signal intensities at varying working distances. To avoid contact with the SERS solution, the distal end of the device was brought no closer than ~7 mm. (e) Unmixed weighting factors of equimolar (50 pM) and stepwise (5 to 30 pM) mixtures of six different SERS flavors in a 96-well plate (weighting factors calibrated to the equimolar mixture). (f) Ratio of the SERS flavors relative to S493.

the measured ratio of S440 to S493 over working distances up to 55 mm. Nine measurements, spaced 1.0 mm apart in a 3 × 3 grid, were taken at each of the working distances beginning with 7 mm from the sample. The device output power was 60 mW, and an integration time of 300 ms was used. A micrometer gauge was used to incrementally increase the distance of the device from the sample, but there was an error of about ±1 mm in the initial position of the device due to visual estimation of distance. However, the scaled fitting of the experimental data to the FRED model [Fig. 2(c)] suggests adequate positioning of the device relative to the sample. Additionally, six different SERS flavors were placed in wells of a 96-well plate at varying concentrations [Figs. 4(e) and 4(f)]. The first well contained an equimolar mixture of 50 pM of S493, S440, S482, S420, S481, and S421. The second well contained a stepwise mixture of 5-pM S493, 10-pM S440, 15-pM S482, 20-pM S420, 25-pM S481, and 30-pM S421. Spectral measurements from a well filled with MES and an empty well were used as background sets. Spectra from the well containing the equimolar concentrations were unmixed and used to calibrate weighting factors for

each flavor. The calibrated weighting factors were then used to quantify the relative amounts of each SERS flavor in the stepwise mixture.

## 2.6 Unmixing Algorithm

The Raman spectra are produced by the summation of the spectral intensities at each wavelength when the CCD performs FVB. Each Raman spectrum acquisition is then entered into an algorithm to extract the Raman signal of individual SERS flavors. The algorithm used is as follows:  $\vec{w} = \vec{m} * R^+$ , where  $R$  is the reference matrix (a matrix of known SERS spectra and backgrounds),  $\vec{m}$  is the measured Raman spectrum, and  $w$  is a vector of coefficients, or weights, representing the quantity of each component. Each measured Raman spectrum is assumed to be a linear combination of the vectors in the reference matrix. Thus, the vector of weights contains elements,  $w_i$ , corresponding to the relative fraction of each of the reference vectors in  $R$  present in the measured Raman spectrum. Since  $R$  is not a square matrix, the Moore-Penrose pseudoinverse<sup>43</sup>

is used,  $R^+ = R' * (R * R')^{-1}$ , to obtain weights that best fit the references to the data in a least-squares sense. Here we introduce a combination of least squares and PCA to obtain reference spectra for background signals caused by sources other than nanoparticles, such as the device optics, stray light, and the intrinsic Raman scatter from tissue. The reference matrix has the following entries:

$$R = \begin{bmatrix} SERSflavor \\ mBkgd \\ PC \\ poly \end{bmatrix}, \quad mBkgd = \begin{bmatrix} \overline{BkgdSet_1} \\ \overline{BkgdSet_2} \\ \vdots \\ \overline{BkgdSet_n} \end{bmatrix},$$

$$PC = \begin{bmatrix} PCA(BkgdSet_1) \\ PCA(BkgdSet_2) \\ \vdots \\ PCA(BkgdSet_n) \end{bmatrix}. \quad (6)$$

The first component of the overall reference matrix, *SERSflavor*, is an  $m$ -by- $n$  matrix of measured spectra for each SERS flavor at a known concentration, where  $m$  is the number of flavors used and  $n$  is the number of wavelength bins recorded by the spectrometer CCD. In the experiments discussed in this manuscript, at least two SERS flavors were used: S440 and S493. S493 has a high degree of orthogonality and nearly equal signal strength when compared with S440 (Fig. 3). The degree of orthogonality of the spectra of SERS flavors is an important consideration because overlap in spectra can lead to crosstalk between the signals at low concentrations, which represents an advantage over fluorescence. Identification of 10 different SERS nanoparticles colocalized has been previously reported.<sup>34</sup>

The second component of the reference matrix is the mean background matrix, *mBkgd*. To characterize background signals for unmixing, multiple measurements of each background type (e.g., quartz slide or tissue) are taken and grouped as sets, *BkgdSet<sub>i</sub>*. The spectra from each set, representing a single background type, are averaged and included in *mBkgd* as references. For experiments using tissue biopsies on parafilm (see Sec. 2.9), two background sets were acquired: one of the parafilm and one of the untreated tissue biopsy. In the clinic, only one background set is necessary: the background set of the colon wall prior to the topical application of SERS nanoparticles. Additional background sets may be taken for special purposes, such as a xenon lamp measurement to allow Raman detection with the colonoscope light on.

The third entry in the reference matrix is *PC*, a matrix of principal components from each of the background sets *BkgdSet<sub>i</sub>*. PCA decomposes the  $j$  spectra in the set into  $k < j$  orthogonal vectors that minimize mean square error when used to best fit the original, larger set. For example, subtle variations in colon tissue background signal may be captured by a very large background set and reduced to a few key principal components. The number of principal components used for each background set can be specified in the GUI that interfaces with the device.

The final entry in the reference matrix is a set of polynomials, *poly*, ranging from 0'th to  $n$ 'th order, which accounts for drifts or subtle variations in background signal that are not part of a measured background set. We used a third-order polynomial to

account for slight variations in the measured Raman spectra; a high-order polynomial permits excessive variation in the measured spectra and, therefore, was not used.

The weighting of each of the SERS flavors is given by  $\vec{w}$ ; thus, if *SERSflavor<sub>1</sub>* is the reference spectrum of S440, then the weighting factor of S440 is  $w_1$ . Similarly,  $w_2$  is the weighting factor for *SERSflavor<sub>2</sub>*, the reference spectrum for S493. Variations of similar algorithms compared to the least-squares algorithm have previously been described.<sup>44</sup>

## 2.7 LabView Graphical User Interface

A custom LabView (National Instruments) GUI was developed [Figs. 5(e) and 6(d)] to enable real-time Raman ratiometric imaging and to control key system parameters. The GUI synchronizes the computer with the CCD camera and x-y translation stage (Zaber, T-LSR300A). It then raster scans a user-defined area and step size for a user-defined acquisition time per pixel. The GUI also allows for simple uploading of the S440 and S493 reference spectra and background sets. The value of the weighting factor for each of the respective SERS flavors represents a signal intensity, which is used to create an image while a sample is raster scanned. The image of the individual flavors as well as the ratiometric image is displayed in real time by the GUI. The raw weighting factors of S440 and S493, and the ratiometric images, are scaled such that the entire display range (i.e., 0 to 255) is utilized. At completion of the scan, the LabView software saves all raw data as well as the S440, S493, and ratiometric images for future reference.

## 2.8 Real-Time, Ratiometric Imaging Characterization

In Fig. 5(a), three mixtures of varying concentrations of S440 and S493 are depicted in the lower left column. Droplets of the S440 control are present in the right column, and the upper left droplet is the S493 control. The droplets were added to parafilm supported by a quartz slide. MES buffer was used to dilute all samples.

For the images in Figs. 5(b) and 5(e), two background sets were taken: the parafilm and an 8- $\mu$ L droplet of MES on parafilm. The first five principal components of the parafilm background set and the first six principal components of the MES background set were used in the unmixing algorithm. In Figs. 5 to 7, the laser was set to a power of 60 mW, and the sample was raster scanned with a step size of 700  $\mu$ m and an integration time of 300 ms per pixel.

## 2.9 Real-Time Ratiometric Imaging on Human Colon Tissue

De-identified human colon tissue biopsies  $\sim$ 5 mm in diameter were obtained. The biopsies were immersed for 10 min either in MES, a 1:1 mixture of 5-pM S440 and S493, or a 2:1 mixture of 10-pM S440 and 5-pM S493 [Fig. 6(a)]. MES was used to dilute the nanoparticles. The samples were removed from immersion, placed on parafilm supported by a quartz slide, and imaged in real time [Video 1 of Fig. 5(e) and Video 2 of Fig. 6(d)]. Two sets of backgrounds were taken prior to the scan: one of the parafilm and one of a tissue sample immersed in MES. The first five principal components of the parafilm background set and the first six principal components of the MES background set were used in the algorithm.

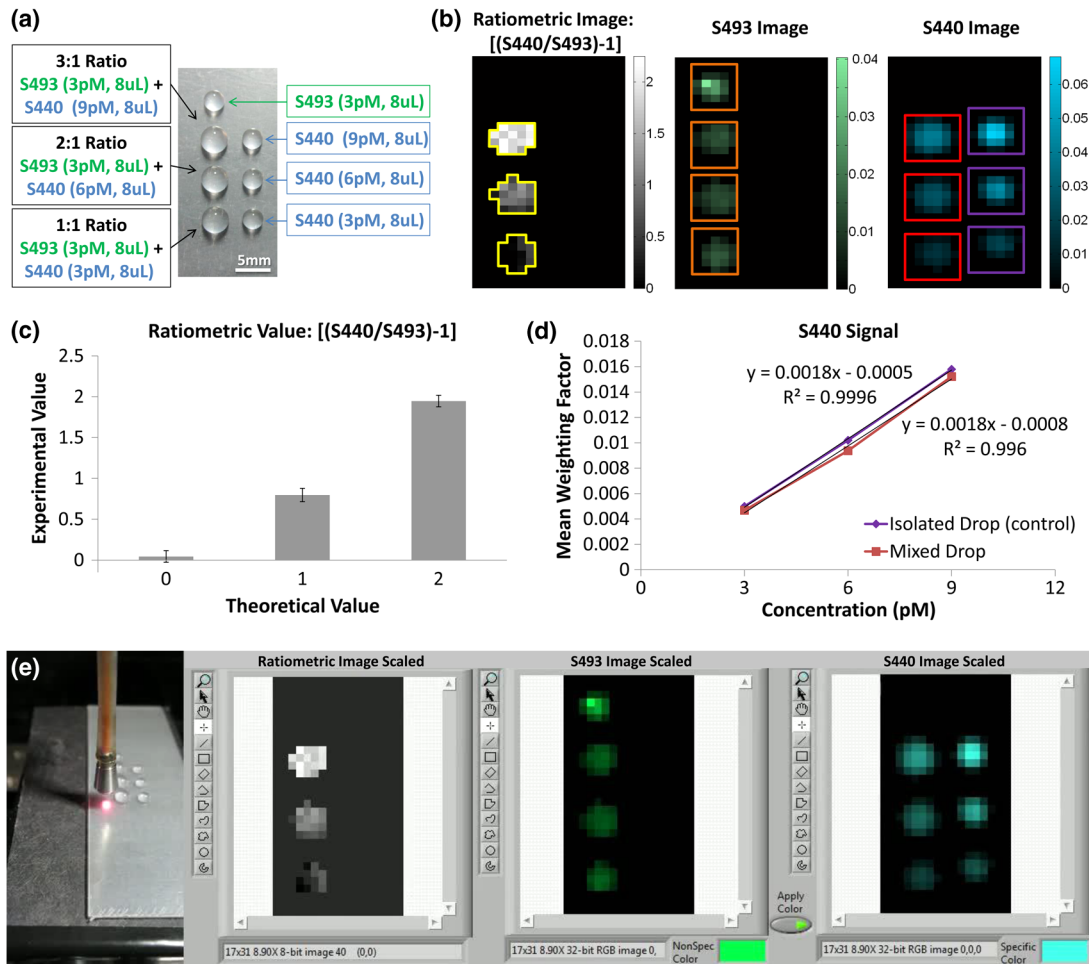


**Fig. 5** (a) Experimental design for real-time ratiometric imaging characterization. (b) The signal intensities of S440 (right), S493 (middle), and the ratiometric value (left). Also shown are the outlines of the regions of interest (ROIs) used for analysis. ROIs depicted by the red squares indicate the S440 signal in droplets where both S493 and S440 SERS nanoparticles are located. The ROIs depicted by the purple squares indicate the S440 signal from the S440-only control samples. (c) Quantification of the ratiometric value within the ROI as shown in (b), left. The error bars are standard errors of the mean,  $\sigma/\sqrt{n}$ , where  $n$  is the number of pixels within each of the ROIs:  $n = 17$  for the ratiometric value of 0,  $n = 18$  for the ratiometric value of 1, and  $n = 16$  for the ratiometric value of 2. (d) Quantification of the S440 signal within the ROI as shown in (b), right. The average Raman signal from the S440-only droplets matched well with the S440 signal from the droplets containing both S440 and S493. (e) Video 1: LabView GUI capable of processing and displaying the signals from each flavor and the ratiometric value in real time as the sample is being scanned. Video played at 2x speed. (Video 1, QuickTime, 12 MB) [URL: <http://dx.doi.org/10.1117/1.JBO.18.9.096008.1>]

Additional human colon tissue biopsies were immersed for 20 min in Eppendorf tubes containing (1) pure MES buffer, (2) an equimolar mixture of 50-pM S493, S440, S482, S420, S481, and S421, (3) a stepwise mixture of 10-pM S493, 20-pM S440, 30-pM S482, 40-pM S420, 50-pM S481, and 60-pM S421, and (4) a stepwise mixture of 5-pM S493, 10-pM S440, 15-pM S482, 20-pM S420, 25-pM S481, and 30-pM S421 [Fig. 7(a)]. Each mixture was chosen to simulate ratiometric imaging of targeted SERS nanoparticles against a nontargeted control (S493). The tissues were placed on a parafilm-covered quartz slide and imaged by using our LabView program. Sets of background images (the empty slide without tissue, the slide with tissue but before incubation in SERS nanoparticles, and a droplet of MES buffer on the slide: 135 spectra total) were first collected, reduced with PCA, and then used to unmix the image of the treated tissues using the algorithm described in Sec. 2.6. Measurements of the equimolar mixture after tissue immersion were used to calibrate the weighting factors and quantify SERS flavor ratios. Due to the current state of

the LabView program, which currently displays two flavors, the images containing six flavors of SERS nanoparticles were postprocessed in MATLAB. When quantifying ratiometric values of each flavor against S493, pixels for which the S493 signal was below 3% of its maximum value were set to zero ratiometric value.

### 3 Results and Discussion

#### 3.1 Optimizing the Raman Endoscope

We found that the best optical components for reducing the background noise produced by the device were (1) multimode fibers whose polyimide coatings had been stripped away at the proximal end of the bundle, (2) the use of opaque epoxy to glue the fibers together at the proximal end, and (3) the use of a fused silica lens with a “deep-V” antireflection coating.

Short et al., demonstrated the importance of coating the illumination fiber to prevent leakage of laser photons into the

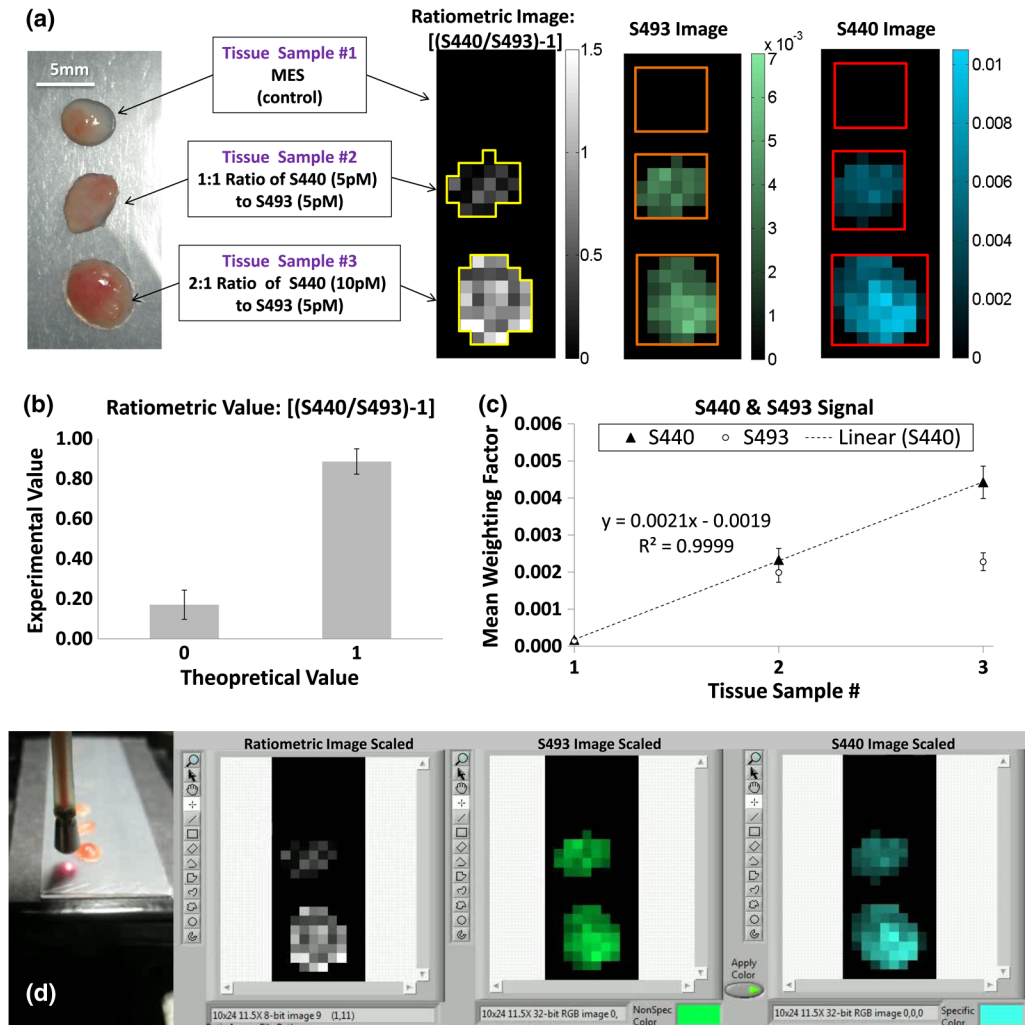


**Fig. 6** (a) The experimental design (left) using human colon tissue biopsies incubated in MES, a 1 : 1 ratio of 5 pM of S440 and S493, or a 2 : 1 ratio of 10 pM of S440 and 5 pM of S493. The resulting ratiometric values of the tissue samples after raster scan are shown on the right. Outlines of the ROIs used for analysis are shown in yellow. (b) Quantification of the ratiometric values within the ROIs as shown in (a), right. The error bars are standard errors of the mean,  $\sigma/\sqrt{n}$ , where  $n$  is the number of pixels within each of the ROIs:  $n = 21$  for the ratiometric value of 0 and  $n = 35$  for the ratiometric value of 1. (c) Quantification of the S440 and S493 signal within the ROI as shown in (a), right. The error bars are the standard error of the mean. (d) Video 2: LabView GUI played at 2 $\times$  speed. (Video 2, QuickTime, 13.5 MB) [URL: <http://dx.doi.org/10.1117/1.JBO.18.9.096008.2>]

collection fibers.<sup>23</sup> However, this crosstalk is negligible in our system because we use a single-mode fiber with bend losses that are much lower than multimode fibers such as the one used by Short et al. Also, our multimode collection fibers have polyimide coatings at the distal end that further reduce crosstalk. We also found that laser light captured and guided by the polyimide coatings of the multimode fibers generated noise at red-shifted wavelengths, which would bypass our long-pass filter and generate a background signal [see Fig. 1(b), which shows the output of a multimode fiber when illuminated with laser light and filtered with a long-pass filter]. The source of the red-shifted noise is probably fluorescence or Raman scattering within the polyimide material. Thus, a key design feature of our device is the stripping of the coating of the multimode fibers at the proximal end of the fiber bundle and encapsulation by opaque epoxy. This design modification reduced the amount of laser light and associated noise that was previously reflected into the coating from entering the spectrometer and ultimately the detector [Fig. 1(c)].

An additional source of background noise was the glass material of the plano-convex lens, which is used to both collimate the beam and collect scattered Raman light. Our results show that a fused silica lens—as opposed to quartz, BK7, or SK2—produces the least amount of background signal [Fig. 1(d)] and was thus selected for the lens material. The first surface that the illumination beam contacts after exiting the single-mode fiber is the flat surface of the lens. Rays can reflect off of this surface and backscatter into the multimode collection fibers, ultimately contributing to the background signal. We determined that a deep-V antireflection lens coating, as opposed to a standard broadband coating, further reduces this effect [Fig. 1(e)]. Between a Raman shift of 1100 and 1800  $\text{cm}^{-1}$ , the mean background signal for fused silica with a deep-V coating was 372 counts (as measured by the CCD camera); thus, the lens material selection and coating alone results in a 52% reduction relative to BK7 (mean background = 780 counts), and a 27% reduction relative to SK2 (mean background = 507 counts).

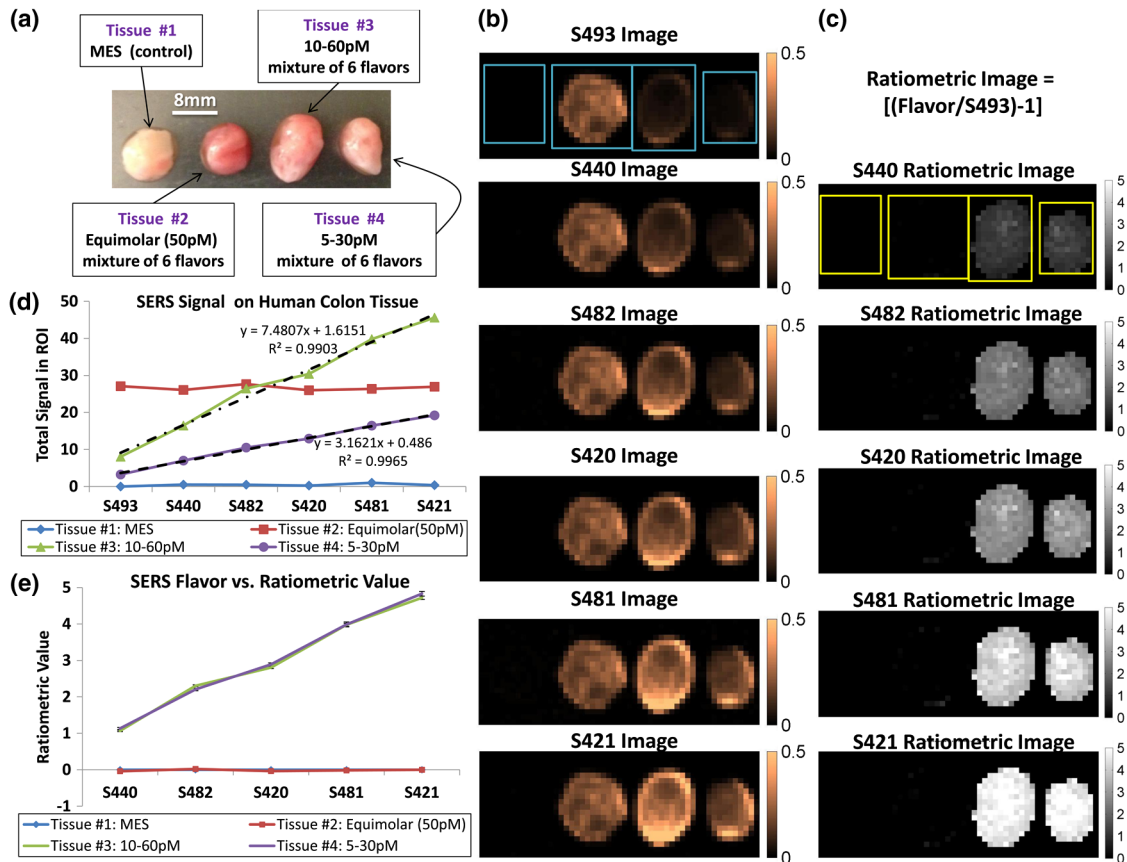


**Fig. 7** (a) Human colon tissue biopsies after incubation in MES (left), an equimolar mixture 50 pM of S493, S440, S482, S420, S481, and S421 (left center), a mixture of 10-pM S493, 20-pM S440, 30-pM S482, 40-pM S420, 50-pM S481, and 60-pM S421 (right center), and a mixture of 5-pM S493, 10-pM S440, 15-pM S482, 20-pM S420, 25-pM S481, and 30-pM S421 (right). (b) Image of signal intensities of S493, S440, S482, S420, S481, and S421. Also shown are the ROIs used for analysis. (c) Ratiometric image of the tissue samples. ROIs used for analysis are shown in yellow. (d) Total signal for each of the respective SERS flavors in each tissue sample ROI from (b). (e) Average of nonzero ratiometric values for each of the respective SERS flavors in each tissue-sample ROI from (c). Error bars are standard errors of the mean.

### 3.2 Limit of Detection

These optimizations significantly improved the SNR of the system, thereby allowing the detection of SERS nanoparticles of concentrations in the mid femtomolar range to low picomolar range [Fig. 1(f)]. In the well-plate experiments, 291 fM was detected at least one standard deviation above the mean background signal, and 437 fM was detected three standard deviations above the mean background signal. With a 3-mL sample in a 9.5-cm<sup>2</sup> well, the 1.4-mm-diameter beam interrogates a 3.2-mm-deep column of nanoparticles. With a Gaussian beam effective area of  $A_{\text{eff}} = \pi D_s^2/8 = 0.79 \text{ mm}^2$ , the 2.5- $\mu\text{L}$  interrogated volume at 291 fM corresponds to 440,000 nanoparticles. Therefore, using this analytical model, we predict that a tumor tissue composed of 100  $\mu\text{m}^2$  cells could be detected if just 56 functionalized nanoparticles were specifically bound to each cell. 100  $\mu\text{m}^2$  is equivalent to the cross-sectional area of  $\sim 9000$  particles. The ability to detect such low concentrations of SERS nanoparticles is likely required for the clinical translation of our technology.

### 3.3 Collection Efficiency Simulation Results

The simulation of collection efficiency versus distance using FRED software with a plano-convex lens and the ideal lens models (both in FRED and using our own analytical calculation)

were highly congruent; however, two discrepancies were observed: a peak in signal occurring at  $\sim 10 \text{ mm}$  and a slight decrease in signal at an object distance  $> 15 \text{ mm}$  [Fig. 2(c)]. These discrepancies are due to the spherical surface of the plano-convex lens resulting in spherical aberrations. In contrast to the ideal lens, the plano-convex lens bends the scattered Raman rays closer to the center of the fiber bundle. Thus, at an object distance of  $< 15 \text{ mm}$ , the plano-convex lens bends more scattered rays into the detecting multimode fibers, resulting in a higher signal. At an object distance  $> 15 \text{ mm}$ , the plano-convex lens bends a portion of the scattered rays into the nondetecting region occupied by the central illumination fiber, resulting in a lower signal. The FRED simulation utilizing the nonideal, plano-convex lens matches well with experimental measurements of collected Raman scatter versus distance, where only a constant scale factor was used to fit the data to the theoretical curve [Fig. 2(c)].

### 3.4 Evaluating the Ratiometric Approach to Signal Quantification

Our strategy of using SERS nanoparticles allows for the ability to simultaneously multiplex a panel of up to 11 SERS flavors. However, there are two significant shortcomings in a system that does not use at least one SERS flavor as a control. First, the absolute signal from each flavor is inversely correlated with

working distance [Fig. 2(c)], producing variable signal intensities depending upon the position of the endoscope. In clinical practice, it is preferable for the signal to remain relatively constant as the working distance changes, since it can be difficult for a physician to hold the endoscope perfectly still. Second, in the clinic, the wash following topical application of the targeted SERS nanoparticles can result in random accumulation, or pooling, in regions on the surface of the colon. The use of a nontargeted SERS flavor as a control eliminates both of these limitations. In anatomical regions where equal or greater levels of the nontargeted flavor are present, the ratiometric value is equal to zero. In areas where greater levels of targeted SERS flavors are present relative to the nontargeted flavor, the ratiometric value is greater than zero. Thus, the ratiometric value is given by the following equation:

Ratiometric value

$$= \begin{cases} 0, & \text{if } w_{\text{nontargeted}} > w_{\text{targeted}} \\ \frac{w_{\text{targeted}}}{w_{\text{nontargeted}}} - 1, & \text{if } w_{\text{nontargeted}} \leq w_{\text{targeted}} \end{cases} \quad (7)$$

Here,  $w_{\text{targeted}}$  is the weighted value of the targeted flavor and  $w_{\text{nontargeted}}$  is the weighted value of the nontargeted flavor. Thus, the valuable information is no longer the absolute signal of a given SERS flavor but rather the intensity of an SERS flavor of interest relative to the control flavor. Although we are in the process of gaining regulatory approval by the United States Food and Drug Administration (USFDA), current regulatory restrictions prevent us from administering these nanoparticles in humans. Therefore, we used excised human colon tissue samples to evaluate our ratiometric approach. Since the excised tissue may not be viable for tumor targeting, the nanoparticles were not functionalized; however S440 was designated as the targeted flavor and S493 as the nontargeted control flavor in the experiments described in Figs. 4 to 7.

Figure 4(a) demonstrates the signal variance of each individual flavor in response to changes in working distance when the ratio of S440 to S493 is 1:1. This could represent an area of random pooling, for instance, where the relative concentrations of S440 and S493 are equal. Figure 4(c) shows the individual signal intensities varying with distance where the ratio of S440 to S493 is 2:1. This could represent an area where more of the S440 targeted flavor is present than the nontargeted S493, due to an increase in specific binding to the cell receptor of interest. It is important to note that although the absolute value of each flavor decreases with working distance [Figs. 4(a) and 4(c)], the ratio of S440/S493 remains constant [Figs. 4(b) and 4(d)]. The standard deviation of the ratio (noise) does increase as the working distance increases. This result demonstrates the benefit of ratiometric imaging for controlling signal variances that can occur in response to changes in working distance. Six SERS flavors were also evaluated in a well plate [Figs. 4(e) and 4(f)]. The ratios of five SERS flavors relative to S493 were equal to 1 for the equimolar mixture after calibration. The ratio of the other flavors relative to S493 increased linearly for the 5 to 30 pM stepwise mixture, demonstrating ratiometric detection of six SERS flavors simultaneously [Fig. 4(f)].

Additionally, varying ratios of S440 to S493 were mixed at single-digit picomolar concentrations and pipetted in low volumes onto parafilm (Fig. 5). Ratios of 3:1, 2:1, and 1:1 of S440 to S493 were evaluated, resulting in ratiometric values of 2, 1, and 0, respectively [Fig. 5(c)]. Although we measured a

maximum ratio of 3:1, in cases where the ratio is higher—that is, when washing is more perfect—the signal of the targeted flavor is more relevant to quantify binding. The mean S493 signal within the regions of interest (ROIs) did not vary by more than 15% between the signal obtained from the control droplet and the signal obtained from the mixed droplets [Fig. 5(b), middle]. For a ratiometric value of 0, 1, and 2, the mean value was 0.04, 0.80, and 1.95, respectively. The error bars shown in Fig. 5(c) are the standard error of the mean with lengths of 0.29, 0.32, and 0.28, respectively. The signals within the ROIs are quantified in Fig. 5(d) and demonstrate that the average Raman signal in the S440 isolated droplets matched well with the S440 signal from the mixed droplets containing both S440 and S493. This confirms that, in addition to the ability to detect flavors that are mixed together, the presence of one flavor does not affect the intensity of the other.

To evaluate the ratiometric technique on tissue, human colon biopsies were immersed in varying ratios of S440 to S493 (Fig. 6). One tissue sample was immersed in a 1:1 ratio to model an area of random pooling of targeted and nontargeted SERS particles on tissue. Another tissue sample was immersed in a 2:1 ratio of S440 to S493 to model an area of targeted binding where more S440 is present than S493. For a ratiometric value of 0 and 1, the mean value was 0.17 and 0.89, respectively. The error bars shown in Fig. 6(b) are the standard error of the mean, which are 0.07 and 0.06, respectively. The ability to image the SERS signals and ratiometric values in real time on a slide [Video 1 of Fig. 5(e)] and on human colon tissue [Video 2 of Fig. 6(d)] was also demonstrated.

Human colon biopsies after immersion in varying ratios of six different SERS flavors are shown in Fig. 7(a). The experiment simulates binding of five targeted SERS nanoparticle flavors (S440, S482, S420, S481, and S421) and a nontargeted control flavor (S493). Tissue #2, immersed in an equimolar 50-pM mixture, models an area of random pooling of targeted and nontargeted nanoparticles. Tissues #3 and #4, immersed in 1:2:3:4:5:6 ratios of S493:S440:S482:S420:S481:S421, model areas of targeted binding where more of the targeted flavors are present relative to S493 (e.g., five different protein markers, each overexpressed in different amounts on the tissue surface). The ability to image the six SERS signals and perform ratiometric analysis on human colon tissue was demonstrated. Figures 7(b) and 7(d) show images and quantified signal levels from each of the respective flavors. Tissue #2 expressed equal signal for all flavors, while tissues #3 and #4 expressed increasing intensities as predicted by their respective immersions. Nonuniformity in signal strength is evident from Fig. 7(b), due to topography of the tissue samples (having thicknesses up to 5 mm) and pooling of nanoparticles around the tissue edges. However, when quantified ratiometrically [image in Fig. 7(c) and quantification in Fig. 7(e)], the nonuniformity is largely mitigated due to the ratiometric analysis, and ratiometric values agree with predictions.

### 3.5 Clinical Translation Benefits of Using Principal Component Analysis

With the PCA approach described here, multiple background sets can be included when required. For instance, when the SERS nanoparticles were pipetted onto parafilm (Fig. 5), one background set was taken on parafilm only and another on a pure-MES sample placed on parafilm. Similarly, with the human colon tissue experiments (Fig. 6), one background set

was taken on parafilm only and another on tissue washed in MES. The advantage of PCA is that it allows for large background sets to be taken, if needed, in order to capture and extract the distinguishing characteristics of a given background type and variations thereof. This is an important feature in the clinical setting because it enables full characterization of the background Raman signal for a given patient with a minimum number of principal component vectors. Utilizing more components than the minimum necessary to best fit the set will introduce noise in the algorithm and increase the fitting error. In the experiments depicted by Figs. 4 and 5, no more than the first six primary principal components were used for any given background set; principal components beyond the first six were similar to the noise floor and, therefore, were not used.

### 3.6 Graphical User Interface and Real-Time Analysis

Many of the SERS techniques described in the past have required postprocessing of data sets.<sup>13,14</sup> Real-time analysis, as demonstrated here (Figs. 5 and 6), is a necessity for point-of-care detection and potential therapy. Our system displays the weighted values of each SERS flavor and the ratiometric value in real time as the samples are scanned [Video 1 of Fig. 5(e) and Video 2 of Fig. 6(d)]. In the clinical setting, these ratiometric values can be visually and audibly displayed in real time, providing immediate diagnostic feedback. An abundance of a targeted SERS nanoparticle flavor relative to the control, nontargeted flavor would result in an increase in the ratiometric value. This allows for localization of suspicious regions as well as quantification of the relative binding of the SERS nanoparticles to their biomarker targets. In addition, real-time analysis with our system enables the use of bedside raster scanning and image generation of biopsies prior to sending them to pathology for confirmation.

### 3.7 System Overview

Our Raman endoscope offers practical advantages for clinical detection of SERS nanoparticles. First, the illumination laser is collimated, enabling a detection resolution that is independent of working distance and a constant power density that can be reliably kept below maximum permissible energy limits. Our system has a small profile that enables it to be deployed through the working channel of a clinical endoscope. The 785-nm laser of our device was visible on the CCD camera image of the endoscope, enabling direct correlation of detected Raman signal with anatomic information.<sup>34</sup> Second, by measuring the entire spectrum with each acquisition and unmixing with our least-squares and PCA algorithm, our system can be used for real-time ratiometric quantification of nanoparticles without requiring that the clinician maintain a fixed working distance or hold the endoscope still. The full-spectrum acquisition is also robust against background signals that may overlap with some SERS spectral peaks, e.g., xenon lamp light from the white-light clinical endoscope that would be used to deploy our device.<sup>34</sup> With acquisitions below 1 s per pixel, we believe our system will minimally impact the average withdrawal time in traditional endoscopy and thus have clinical utility.

Although the majority of the background signal in our device comes from the multimode collection fibers and collimating optics, our design is compatible with recent advances in background reduction achieved in the excitation fibers of other Raman devices, including Kagome-lattice hollow-core photonic

crystal fibers (HC-PCF)<sup>45</sup> and low-noise fluorocarbon fibers.<sup>46</sup> Gheuche et al. have shown a background reduction by over two orders of magnitude using HC-PCF when compared to standard silica fibers for the detection of intrinsic Raman signals.<sup>45</sup> Although these fibers have reduced background noise, they are single mode and greatly limit the collection efficiency of Raman scattered light when used as collection fibers. Therefore, further evaluation would be required to determine if an increased SNR could be achieved by using HC-PCF fibers either for illumination or signal collection in our system design for the detection of SERS nanoparticles.

## 4 Conclusions

We report the first demonstration of a real-time, ratiometric endoscopic Raman imaging system utilizing SERS nanoparticles, which is designed to be clinically deployable. The GUI will allow physicians to rapidly identify and visualize various SERS nanoparticle flavors and the corresponding ratiometric values. The device has been optimized to allow for detection and quantification of low concentrations of SERS flavors in the single-digit picomolar range. The multiflavor approach introduced—where at least one flavor is designated as a targeted flavor and one flavor is designated as a nontargeted, control flavor—allows for an internal control and compensates for the signal variation that occurs in response to changes in the working distance. This development of an optimized, noncontact device capable of scanning larger areas of tissue in short periods of time and in locations where the tissue topography varies significantly, such as the colon, is an important step toward effective clinical translation. Topical application of functionalized SERS nanoparticles with detection by an endoscope-deployable, fiber-based, noncontact SERS endoscope device comprises a molecular imaging technology with the potential for early detection of epithelial cancers in hollow organs. Advances in these technologies will enable point-of-care detection and more accurate image-guided resection, predictively leading to an improved quality of life and higher rates of long-term disease-free survival.

To further advance this technology, future work will include testing of the device using functionalized SERS nanoparticles, with targeted and nontargeted nanoparticles to be tested *in vivo* in mouse models. The SERS nanoparticles will also be conjugated to fluorophores as a separate control. Additionally, a second generation of the current device is under development that has an illumination beam that circumferentially scans the internal diameter of the organ lumen, such as the colon. A controlled retraction of the device will help provide a Raman map of the colon depicting the location and concentration of various SERS flavors.

### Acknowledgments

We would like to thank Laura Bronsart for her support. In addition, this work was funded, in part, by The Canary Foundation and grant support from the National Cancer Institute including ICMIC P50 CA114747, CCNE U54 CA119367, and NTR U54 CA136465.

### References

1. R. Siegel, D. Naishadham, and A. Jemal, "Cancer statistics, 2012," *CA Cancer J. Clin.* **62**(1), 10–29 (2012).
2. A. Jemal et al., "Global cancer statistics," *CA Cancer J. Clin.* **61**(2), 69–90 (2011).

3. R. M. Soetikno et al., "Prevalence of nonpolypoid (flat and depressed) colorectal neoplasms in asymptomatic and symptomatic adults," *JAMA* **299**(9), 1027–1035 (2008).
4. J. V. Jokerst and S. S. Gambhir, "Molecular imaging with theranostic nanoparticles," *Acc. Chem. Res.* **44**(10), 1050–1060 (2011).
5. C. L. Zavaleta, M. F. Kircher, and S. S. Gambhir, "Raman's 'effect' on molecular imaging," *J. Nucl. Med.* **52**(12), 1839–1844 (2011).
6. W. E. Doering et al., "SERS as a foundation for nanoscale, optically detected biological labels," *Adv. Mater.* **19**(20), 3100–3108 (2007).
7. M. Fleischmann, P. J. Hendra, and A. J. McQuillan, "Raman spectra of pyridine adsorbed at a silver electrode," *Chem. Phys. Lett.* **26**(2), 163–166 (1974).
8. M. Y. Sha et al., "Surface-enhanced Raman scattering tags for rapid and homogeneous detection of circulating tumor cells in the presence of human whole blood," *J. Am. Chem. Soc.* **130**(51), 17214–17215 (2008).
9. E. Smith and G. Dent, *Modern Raman Spectroscopy: A Practical Approach*, J. Wiley, Hoboken, NJ (2005).
10. K. Kneipp, "Surface-enhanced Raman scattering," *Physics Today* **60**(11), 40 (2007).
11. K. Kneipp, M. Moskovits, and H. Kneipp, *Surface-Enhanced Raman Scattering: Physics and Applications*, Springer, Berlin, New York (2006).
12. C. L. Haynes, A. D. McFarland, and R. P. V. Duyne, "Surface-enhanced Raman spectroscopy," *Anal. Chem.* **77**(17), 338-A (2005).
13. S. Keren et al., "Noninvasive molecular imaging of small living subjects using Raman spectroscopy," *Proc. Natl. Acad. Sci. USA* **105**(15), 5844–5849 (2008).
14. C. L. Zavaleta et al., "Multiplexed imaging of surface enhanced Raman scattering nanotags in living mice using noninvasive Raman spectroscopy," *Proc. Natl. Acad. Sci. USA* **106**(32), 13511–13516 (2009).
15. X. M. Qian and S. M. Nie, "Single-molecule and single-nanoparticle SERS: from fundamental mechanisms to biomedical applications," *Chem. Soc. Rev.* **37**(5), 912–920 (2008).
16. A. S. Thakor et al., "The fate and toxicity of Raman-active silica-gold nanoparticles in mice," *Sci. Transl. Med.* **3**(79), 79ra33 (2011).
17. A. S. Thakor et al., "Oxidative stress mediates the effects of Raman-active gold nanoparticles in human cells," *Small* **7**(1), 126–136 (2011).
18. C. L. Zavaleta et al., "Preclinical evaluation of Raman nanoparticle biodistribution for their potential use in clinical endoscopy imaging," *Small* **7**(15), 2232–2240 (2011).
19. M. G. Shim et al., "In vivo near-infrared Raman spectroscopy: demonstration of feasibility during clinical gastrointestinal endoscopy," *Photochem. Photobiol.* **72**(1), 146–150 (2000).
20. Z. Huang et al., "Raman spectroscopy of *in vivo* cutaneous melanin," *J. Biomed. Opt.* **9**(6), 1198–1205 (2004).
21. Z. Huang et al., "Rapid near-infrared Raman spectroscopy system for real-time *in vivo* skin measurements," *Opt. Lett.* **26**(22), 1782–1784 (2001).
22. Z. Huang et al., "Near-infrared Raman spectroscopy for optical diagnosis of lung cancer," *Int. J. Cancer* **107**(6), 1047–1052 (2003).
23. M. A. Short et al., "Development and preliminary results of an endoscopic Raman probe for potential *in vivo* diagnosis of lung cancers," *Opt. Lett.* **33**(7), 711–713 (2008).
24. Y. Komachi et al., "Micro-optical fiber probe for use in an intravascular Raman endoscope," *Appl. Opt.* **44**(22), 4722–4732 (2005).
25. A. Mahadevan-Jansen et al., "Near-infrared Raman spectroscopy for *in vitro* detection of cervical precancers," *Photochem. Photobiol.* **68**(1), 123–132 (1998).
26. A. Mahadevan-Jansen et al., "Development of a fiber optic probe to measure NIR Raman spectra of cervical tissue *in vivo*," *Photochem. Photobiol.* **68**(3), 427–431 (1998).
27. A. Robichaux-Viehoever et al., "Characterization of Raman spectra measured *in vivo* for the detection of cervical dysplasia," *Appl. Spectrosc.* **61**(9), 986–993 (2007).
28. A. Molckovsky et al., "Diagnostic potential of near-infrared Raman spectroscopy in the colon: differentiating adenomatous from hyperplastic polyps," *Gastrointest. Endosc.* **57**(3), 396–402 (2003).
29. M. V. Schulmerich et al., "Transcutaneous Raman spectroscopy of murine bone *in vivo*," *Appl. Spectrosc.* **63**(3), 286–295 (2009).
30. A. M. Mohs et al., "Hand-held spectroscopic device for *in vivo*, and intraoperative tumor detection: contrast enhancement, detection sensitivity, and tissue penetration," *Anal. Chem.* **82**(21), 9058–9065 (2010).
31. R. J. Mallia et al., "Filter-based method for background removal in high-sensitivity wide-field-surface-enhanced Raman scattering imaging *in vivo*," *J. Biomed. Opt.* **17**(7), 076017 (2012).
32. P. Z. McVeigh et al., "Development of a widefield SERS imaging endoscope," *Proc. SPIE* **8217**, 821704 (2012).
33. P. Z. McVeigh et al., "Widefield quantitative multiplex surface enhanced Raman scattering imaging *in vivo*," *J. Biomed. Opt.* **18**(4), 046011 (2013).
34. C. L. Zavaleta et al., "A Raman-based endoscopic strategy for multiplexed molecular imaging," *Proc. Natl. Acad. Sci. USA* **110**(25), E2288–E2297 (2013).
35. B. R. Lutz et al., "Spectral analysis of multiplex Raman probe signatures," *ACS Nano* **2**(11), 2306–2314 (2008).
36. X. Qian et al., "In vivo tumor targeting and spectroscopic detection with surface-enhanced Raman nanoparticle tags," *Nat. Biotechnol.* **26**(1), 83–90 (2008).
37. J. T. Liu et al., "Quantifying cell-surface biomarker expression in thick tissues with ratiometric three-dimensional microscopy," *Biophys. J.* **96**(6), 2405–2414 (2009).
38. J. T. Liu et al., "Ratiometric 3-D scanning cytometer for quantifying cell-surface biomarker expression within intact tissues," in *Novel Techniques in Microscopy*, Optical Society of America (2009).
39. K. M. Tichauer et al., "Advantages of a dual-tracer model over reference tissue models for binding potential measurement in tumors," *Phys. Med. Biol.* **57**(20), 6647–6659 (2012).
40. J. V. Jokerst et al., "Affibody-functionalized gold-silica nanoparticles for Raman molecular imaging of the epidermal growth factor receptor," *Small* **7**(5), 625–633 (2011).
41. C. Zavaleta et al., "Noninvasive Raman spectroscopy in living mice for evaluation of tumor targeting with carbon nanotubes," *Nano Lett.* **8**(9), 2800–2805 (2008).
42. F. L. Pedrotti, L. M. Pedrotti, and L. S. Pedrotti, *Introduction to Optics*, Pearson/Prentice Hall, Upper Saddle River, NJ (2007).
43. A. Ben-Israel and T. N. E. Greville, *Generalized Inverses: Theory and Applications*, Wiley, New York (1974).
44. D. Van de Sompel et al., "A hybrid least squares and principal component analysis algorithm for Raman spectroscopy," *PLoS One* **7**(6), e38850 (2012).
45. P. Ghenuche et al., "Kagome hollow-core photonic crystal fiber probe for Raman spectroscopy," *Opt. Lett.* **37**(21), 4371–4373 (2012).
46. P. I. Ookagbare and M. D. Morris, "Fluorocarbon fiber-optic Raman probe for non-invasive Raman spectroscopy," *Appl. Spectrosc.* **66**(6), 728–730 (2012).